INTERNATIONAL JOURNAL FOR NUMERICAL METHODS IN FLUIDS
Int. J. Numer. Meth. Fluids 2009; **60**:1173–1199
Published online 20 October 2008 in Wiley InterScience (www.interscience.wiley.com). DOI: 10.1002/fld.1926

Geometrical interpretation of the multi-point flux approximation L-method

Yufei Cao[1,*,†], Rainer Helmig[2] and Barbara I. Wohlmuth[1]

[1]*Institut für Angewandte Analysis und Numerische Simulation (IANS), Universität Stuttgart, Pfaffenwaldring 57, 70569 Stuttgart, Germany*
[2]*Institut für Wasserbau, Lehrstuhl für Hydromechanik und Hydrosystemmodellierung, Universität Stuttgart, Pfaffenwaldring 61, 70569 Stuttgart, Germany*

SUMMARY

In this paper, we first investigate the influence of different Dirichlet boundary discretizations on the convergence rate of the multi-point flux approximation (MPFA) L-method by the numerical comparisons between the MPFA O- and L-method, and show how important it is for this new method to handle Dirichlet boundary conditions in a suitable way. A new Dirichlet boundary strategy is proposed, which in some sense can well recover the superconvergence rate of the normal velocity. In the second part of the work, the MPFA L-method with homogeneous media is studied. A systematic concept and geometrical interpretations of the L-method are given and illustrated, which yield more insight into the L-method. Finally, we apply the MPFA L-method for two-phase flow in porous media on different quadrilateral grids and compare its numerical results for the pressure and saturation with the results of the two-point flux approximation method. Copyright © 2008 John Wiley & Sons, Ltd.

Received 3 June 2008; Revised 15 August 2008; Accepted 19 August 2008

KEY WORDS: multi-point flux; O-method; L-method; convergence; Dirichlet boundary; homogeneous media

1. INTRODUCTION

Single- and multi-phase flow in porous media play an important role in many natural and industrial fields, such as the oil industry where the flow of oil, water and gas in reservoir is studied, or environmental engineering where flow and transport of contaminants in the subsurface are

*Correspondence to: Yufei Cao, Institut für Angewandte Analysis und Numerische Simulation (IANS), Universität Stuttgart, Pfaffenwaldring 57, 70569 Stuttgart, Germany.
†E-mail: yufei.cao.prc@gmail.com

Contract/grant sponsor: DFG; contract/grant number: GRK 1398

considered. The flow system using the fractional flow formulation contains a pressure equation with elliptic behavior, which is linear for single-phase flow and nonlinear for multi-phase flow, see [1].

The finite volume method is a numerical discretization technique, which can locally inherit physical conservation laws of original problems. The property of discrete local mass conservation is desirable to approximate the elliptic operators in the pressure equation for single- and multi-phase flow. Therefore, it is popular in the solution for multi-phase flow in reservoir simulation.

The classical cell-centered finite volume (CCFV) method is a physically intuitive control-volume formulation using the two-point flux approximation (TPFA), which is generally used to approximate elliptic operators in reservoir simulation. However, it is only correct if the grid directions are aligned with the principal directions of the permeability tensor $\mathbf{K}$. For general non-$\mathbf{K}$-orthogonal grids, TPFA does not work properly due to the error in its solution, which cannot be reduced by refining the grids, see [2]. In the reservoir simulation, the grids with a high aspect ratio are quite often used, and the grids with a more complex geometry are preferred at faults or in near-well regions. To overcome this problem, the multi-point flux approximation (MPFA) methods were widely studied in the last decade. It can give a correct discretization of flow equations not only for general non-orthogonal grids but also for general orientation of the principal directions of the permeability tensor.

There are many variants of the MPFA method (see [3]), which are deduced by different continuity conditions, the most popular of which is the O-method. In this method, the transmissibility coefficients are calculated by requiring the pressure continuity at the midpoint of each interface and the flux continuity at the interfaces of the cells in an interaction volume. An introduction to the MPFA O-method for quadrilaterals can be found in [4–9]. Convergence of the O-method is discussed in [7, 10–15]. In particular, the MPFA O-method introduced by Aavatsmark *et al.* [6, 7] will be used for our numerical experiments.

Another important property for multi-phase flow is the monotonicity of the numerical elliptic operator, which can avoid unphysical oscillations in the discrete solution. Conditions for monotonicity of the MPFA on quadrilaterals are discussed in [16]. In order to improve the monotonicity of the MPFA, a new MPFA method called the L-method was introduced for quadrilateral grids in 2D in [17] based on the optimal monotonicity criteria derived in [16], and it was extended to 3D in [18]. The L-method requires full pressure continuity at the interfaces inside each interaction volume, which leads to fewer cells in the flux stencils compared with the O-method, and it has the other two main advantages: a larger domain of convergence and a larger domain of monotonicity. Thus, in this study, we focus on the study of the new MPFA L-method for quadrilaterals in 2D.

The rest of the paper is organized as follows. In Section 2, the MPFA L-method is described and its Dirichlet boundary handling is studied. Section 2.1 gives a brief illustration of the MPFA L-method for a linear problem, such as the single-phase flow. The influence of different Dirichlet boundary discretizations on the L-method is discussed in Section 2.2 by the numerical investigation and comparisons between the MPFA O- and the L-method. Two kinds of discretization strategies are introduced and three numerical examples are studied, which show how the implementations of Dirichlet boundary affect the convergence rate of the pressure and the normal velocity. Section 3 presents a systematic concept and intuitive observations on the L-method with homogeneous media. First, it is proven that the implementation of the MPFA L-method can be simplified in the case of homogeneous media. Based on this simplification, an equivalent criterion is put forward for choosing the proper L triangle to calculate the fluxes. The criterion is then explained from two aspects of view through some geometrical graphs. Some theorems and corollaries are concluded, and the interpretation for the results of one of the numerical experiments in Section 2.2.3 is shown.

DOI: 10.1002/fld

In Section 4, numerical experiments for a simplified two-phase flow problem are implemented using the MPFA L-method on general quadrilateral grids. Simulation results for the pressure and saturation are given and are also compared with the results of the TPFA method. Finally, some conclusions are given in Section 5. The implementation is performed within the multi-scale multi-physics toolbox DuMux [19], which is based on the recently released DUNE framework [20]. The resulting linear systems are solved by the sparse direct solver PARDISO [21].

2. THE MPFA L-METHOD

The main work of the MPFA L-method is to calculate the fluxes through all the cell edges. Obviously, the flux through the each cell edge on the Neumann boundary can be directly given by Neumann boundary conditions. However, for the Dirichlet boundary, different boundary discretizations can be used, which have different influences on the convergence rate of the L-method. In the following two subsections, a brief description of the L-method is given, and the influence of the Dirichlet boundary discretization on the L-method is studied.

2.1. Description of the MPFA L-method

We consider the second-order elliptic equation in 2D

$$-\nabla\cdot(\mathbf{K}\nabla p)=q \quad \text{in } \Omega\in\mathbb{R}^2 \tag{1}$$

where $\mathbf{K}$ is the conductivity tensor and is assumed to be symmetric and positive definite. In the context of reservoir simulation, problem (1) is the pressure equation for single-phase steady flow in porous media. Correspondingly, $\mathbf{K}$ is the ratio of the intrinsic permeability tensor and the fluid viscosity, and p represents the pressure. The MPFA L-method for Equation (1) on a quadrilateral grid was first introduced and well described in [17]. For completeness, here, we shortly illustrate the L-method on a quadrilateral grid in the following three steps:

(i) Choose a proper L triangle, as shown in Figure 1, either L triangle 1 or L triangle 2 to calculate the transmissibility coefficients t_i^j of a half edge, such as the top half edge $\overline{\bar{x}_1\bar{x}_3}$ between cell 1 and cell 2 in Figure 1. Here, L triangle 1 and L triangle 2 are shortly denoted as T_1 and T_2, respectively; $j=1,2$ indicate that T_j is applied in the computation; i is the cell index, as shown in the figure, $i=1,\ldots,4$; $x_i, i=1,\ldots,4$ are cell centers; $\bar{x}_k, k=1,2$ are midpoints of the edges; and $\bar{x}_3$ is the common corner of the four cells. Let the pressure value at cell center x_i be p_i, and the pressure values at $\bar{x}_k, k=1,2,3$ are denoted by $\bar{p}_k$. In each of the three subcells of an L triangle, for example in T_1, which are the quadrilateral $x_1\bar{x}_1\bar{x}_3\bar{x}_2$, $\triangle\bar{x}_1x_2\bar{x}_3$ and $\triangle\bar{x}_2x_3\bar{x}_3$, linear pressure functions are applied. The pressure values $\bar{p}_k, k=1,2,3$ can be eliminated in the expression of the flux through each half edge by the two continuity conditions: (a) full pressure continuity, (b) flux continuity at the two interfaces (such as, in T_1, $\overline{\bar{x}_1\bar{x}_3}$ and $\overline{\bar{x}_2\bar{x}_3}$) inside a L triangle. Finally, the flux through each half edge can be explicitly expressed by the linear combination of the pressures at the three cell centers, which forms the L triangle with the transmissibility coefficients; that is, for T_1, $f=t_1^1p_1+t_2^1p_2+t_3^1p_3$, and for T_2, $f=t_1^2p_1+t_2^2p_2+t_4^2p_4$. For the detailed deduction of the flux expression, see [17]. The criterion for choosing the proper L triangle is: if $|t_1^1|<|t_2^2|$, choose T_1; otherwise, choose T_2.

DOI: 10.1002/fld

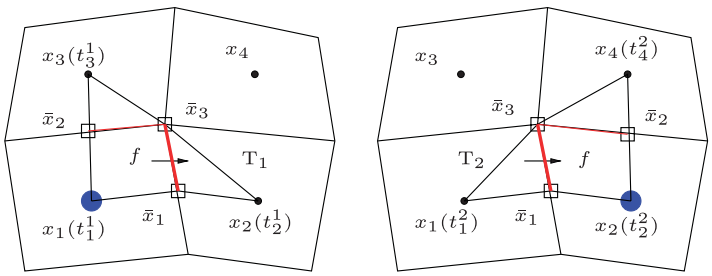

Figure 1. L triangle 1 (T_1, left) and L triangle 2 (T_2, right) for the MPFA L-method.

(ii) Use the procedure in (i) to calculate the fluxes f_1^1 and f_1^2 through two half edges, then the flux f_1 through an entire edge is obtained by the sum $f_1^1 + f_1^2$. Similar to the other three edges of a cell $K \in \mathcal{T}$, $\mathcal{T}$ is the partition of the computational domain Ω.

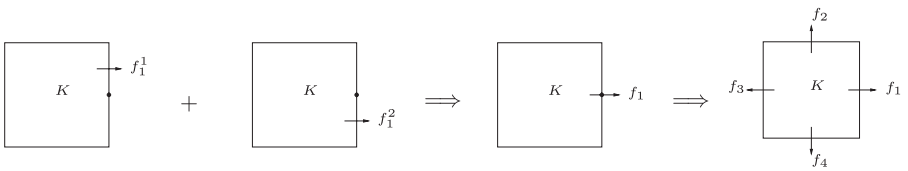

(iii) Insert the four flux expressions derived in (ii) into the local control-volume formulations $f_1 + f_2 + f_3 + f_4 = \int_K q \, \mathrm{d}x$ for all cells $K \in \mathcal{T}$; the discretization of the MPFA L-method is derived.

For 2D, instead of defining pressure continuity points at interfaces in the O-method (see [6, 7]), the L-method requires full pressure continuity at the interfaces inside each interaction volume. It means that only three subcells and two half edges are applied to calculate the transmissibility coefficients for each half edge, whereas four subcells and four half edges are used in the O-method. As mentioned in [17], for homogeneous media and uniform grids, the adaption of the L-method leads to four-point flux stencils for each entire edge and seven-point cell stencils, instead of six-point flux stencils and nine-point cell stencils in the O-method. In fact, the L-method has a better feeling about the direction of the anisotropic tensor than the O-method.

2.2. The influence of the Dirichlet boundary discretization on the MPFA L-method

In this subsection, two kinds of discretization strategies are first introduced for the Dirichlet boundary of the L-method. A numerical investigation between the O- and L-method is then studied to show how important it is for the L-method to handle the Dirichlet boundary implementation in a suitable way. Hence, in the following subsubsections, we only consider the elliptic problem (1) with a homogeneous Dirichlet boundary condition

$$p = 0 \quad \text{on } \Gamma_{\mathrm{D}} = \partial\Omega \tag{2}$$

and a homogeneous permeability tensor $\mathbf{K}$ as our numerical example.

DOI: 10.1002/fld

2.2.1. Dirichlet boundary discretizations of the L-method. The first kind of Dirichlet boundary discretization is originally mentioned in [12, 17], which combines the L-method with the O-method to handle Dirichlet boundary conditions. Thus, we denote this boundary strategy as 'L+O', and correspondingly, the L-method is denoted as 'MPFA L: L+O'. In detail, for all Dirichlet boundary edges, such as $\overline{x_5\bar{x}_2}$ and $\overline{x_6\bar{x}_2}$ in Figure 2 (left) and every second half interior edge connected with the Dirichlet boundary such as $\overline{\bar{x}_2\bar{x}_3}$ in Figure 2 (left), the O-method is applied in the interaction volume covering the Dirichlet boundary such as the quadrilateral $x_1x_2x_6x_5$ in Figure 2 (left) to calculate the fluxes, for the detailed flux computation, see [12]. Meanwhile, for every first half interior edge near the Dirichlet boundary such as $\overline{\bar{x}_1\bar{x}_3}$ in Figure 2 (left), the L-method is implemented to calculate the flux f_1^1 using either $\triangle x_1x_2x_3$ or $\triangle x_1x_2x_4$.

Based on the first boundary strategy, we propose the second kind of Dirichlet boundary discretization, which applies the O-method for both the first and second half interior edges connected with the Dirichlet boundary. For example, in Figure 2 (right), the interaction volume $x_1x_2x_4x_3$ is used to calculate the flux f_1^1 through the first half edge $\overline{\bar{x}_1\bar{x}_3}$, whereas the interaction volume $x_1x_2x_6x_5$ is used to calculate the flux f_1^2 through the second half edge $\overline{\bar{x}_2\bar{x}_3}$. This boundary strategy is denoted as 'full O', and correspondingly, the L-method is denoted as 'MPFA L: full O'.

2.2.2. Rectangular grid with mild anisotropy. As the first numerical example, we consider $q=48x(1-x)-16(1-2x)(1-2y)+48y(1-y)$ and a mild anisotropy $\mathbf{K}$:

$$\mathbf{K}=\begin{pmatrix}1.5 & 0.5\\ 0.5 & 1.5\end{pmatrix} \tag{3}$$

on a rectangular grid, which has the exact solution $p=16x(1-x)y(1-y)$. Since the tensor $\mathbf{K}$ is symmetric, the principal directions are orthogonal. It is easy to see that the two principal directions of the anisotropic full tensor (3) are $\mathbf{k_1}=(1,1)^{\mathrm{T}}, \mathbf{k_2}=(1,-1)^{\mathrm{T}}$ as shown in Figure 3(a), which are not aligned with the rectangular grid directions. Thus, for this tensor $\mathbf{K}$, the rectangular grid is a non-$\mathbf{K}$-orthogonal grid.

Numerical results for the MPFA O-method and L-method on the rectangular grid (see Figure 4 (left)) are shown from the refinement level 1–5. Here, the refinement level of the initial grid is level 0, and the next finer grid on level 1 is constructed by halving all the cells of the initial grid in both the x- and y-direction. Similarly, the grids on level $2, 3, \ldots$ can be obtained successively.

Initially, we implement the 'MPFA L: L+O' method and find out that its convergence rate of the normal velocity is $\mathcal{O}(h^{1.5})$, which loses $\mathcal{O}(h^{0.5})$ in comparison with the O-method, see

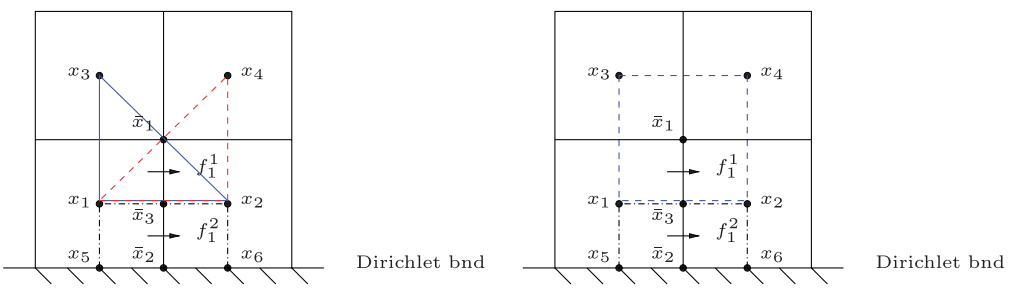

Figure 2. Dirichlet boundary discretizations: 'MPFA L: L+O' (left); 'MPFA L: full O' (right).

DOI: 10.1002/fld

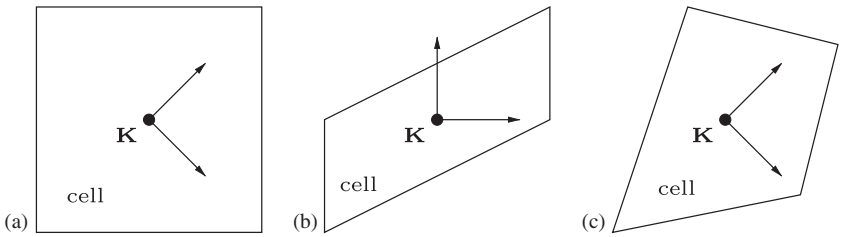

Figure 3. Grid cell with principal directions of the permeability tensor **K**.

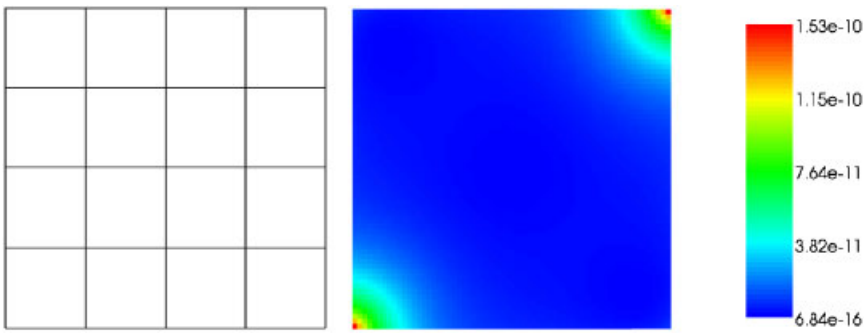

Figure 4. Rectangular grid (left, level 0), local relative error graph for normal velocity of O-method (right, level 4).

Figure 7 (right). In all the convergence-order graphs, $n = 1/h_{\max}$, where '$h_{\max}$' is the maximum of the diameters of all cells. 'e' represents the relative discrete L_2 norm of the error either for the pressure defined by the expression

$$e_p = \left(\frac{\sum_{K \in \mathcal{T}} |K| (p_{\mathrm{ex},K} - p_K)^2}{\sum_{K \in \mathcal{T}} |K| p_{\mathrm{ex},K}^2} \right)^{1/2} \tag{4}$$

or for the normal velocity defined by

$$e_v = \left(\frac{\sum_{K \in \mathcal{T}} \sum_{j \in \partial K} |K| (f_{\mathrm{ex},j} - f_j)^2}{\sum_{K \in \mathcal{T}} \sum_{j \in \partial K} |K| f_{\mathrm{ex},j}^2} \right)^{1/2} \tag{5}$$

Here, the analytical pressure value $p_{\mathrm{ex},K}$ is evaluated at the cell center of K, p_K is the discrete solution of the pressure at the cell center and $|K|$ is the area of the cell K. The analytical normal velocity $f_{\mathrm{ex},j}$ is evaluated by $-\mathbf{K}\nabla p \cdot \mathbf{n}$ at the midpoint of the cell edge j, where $\mathbf{n}$ is the unit outer normal of j. f_j is the discrete normal velocity calculated at the cell edge center.

Figure 4 (right) and Figure 5 (left) show the local relative error for the normal velocity. It can be seen that the 'L+O' strategy gives a much bigger error for the normal velocity on the Dirichlet boundary layer with the magnitude 10^{-8} compared with the error magnitude 10^{-10} for the O-method. If we calculate the error for the pressure and the normal velocity only using the

DOI: 10.1002/fld

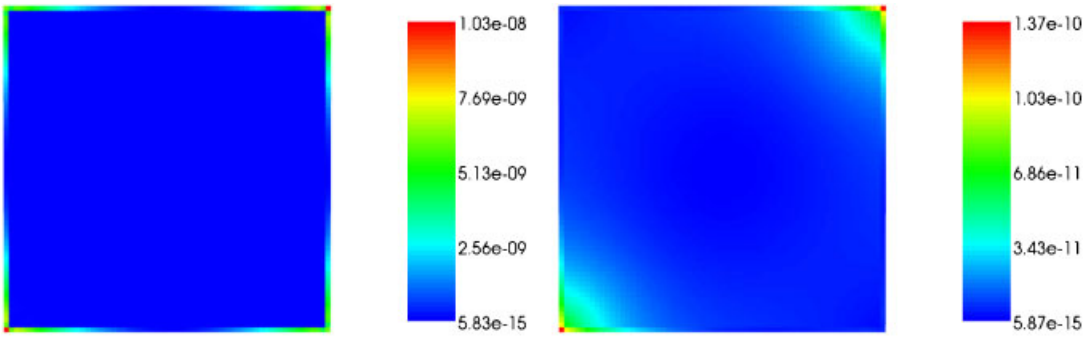

Figure 5. Local relative error graph for normal velocity of L-method: 'L+O' (left, level 4) and 'full O' (right, level 4).

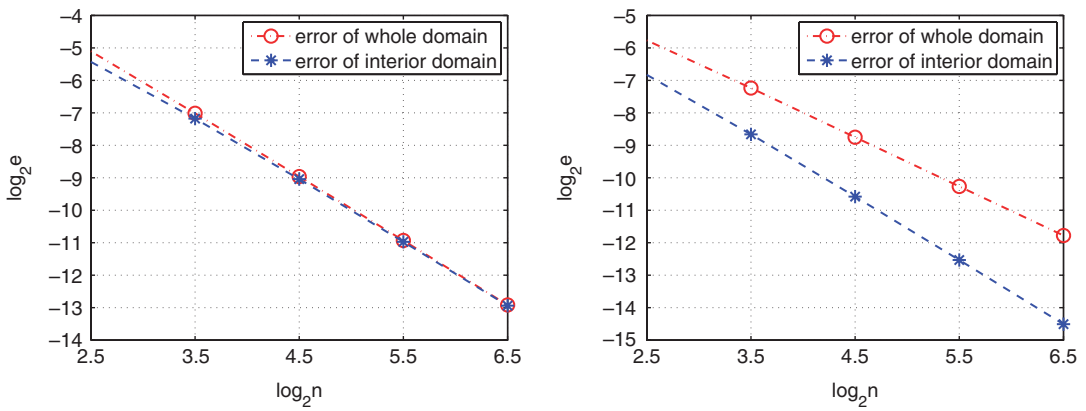

Figure 6. Convergence-order graph on rectangular grid with 'MPFA L: L+O' boundary discretization: pressure (left), normal velocity (right).

interior cells inside the computational domain, from Figure 6 it is easy to see that the convergence rate of the normal velocity increases to $\mathcal{O}(h^2)$ instead of $\mathcal{O}(h^{1.5})$ for the whole domain. But for the pressure, the Dirichlet boundary layer only has a weak influence on the convergence.

Based on the above observation, it motivates us to improve the numerical computation of the Dirichlet boundary cells in the L-method. Therefore, the second kind of Dirichlet boundary discretization mentioned in Section 2.2.1 is introduced in terms of the properties needed by the superconvergence. Figure 7 shows the discrete L_2 convergence behavior of the solution to the problem (1) and (2) using the MPFA O-method, 'L+O' and 'full O' strategy of the L-method. Obviously, the superconvergence rate of the normal velocity is successfully recovered to $\mathcal{O}(h^2)$ by applying the improved boundary performance 'full O'. By the local error graph for the normal velocity in Figure 5 (right), it can also be seen that the big boundary error is well reduced to the same magnitude 10^{-10} as in the O-method. Meanwhile, Figure 7 (left) shows that the convergence order for the pressure is $\mathcal{O}(h^2)$ for all the three numerical methods, which indicates that the boundary implementation of the L-method does not affect the pressure much.

DOI: 10.1002/fld

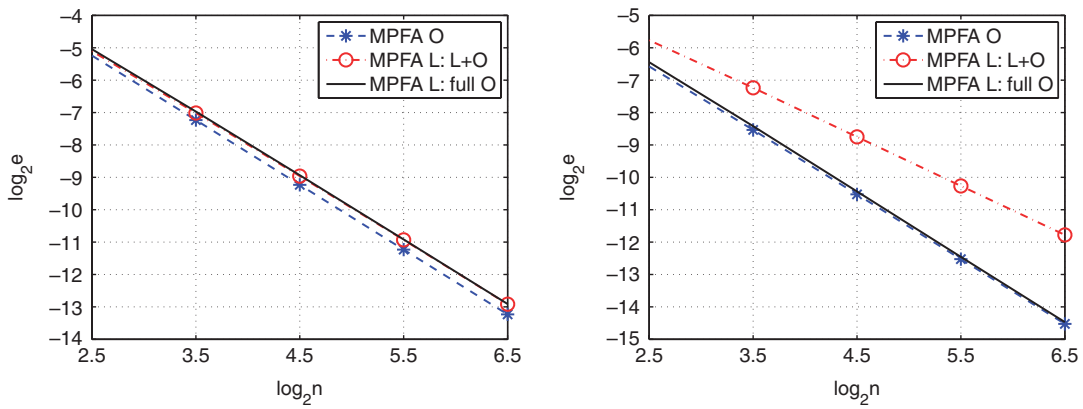

Figure 7. Convergence-order graph on rectangular grid: pressure (left), normal velocity (right).

2.2.3. Quadrilateral grid with isotropy. Furthermore, the numerical example with $q=32x(1-x)+32y(1-y)$ and isotropy $\mathbf{K}$:

$$\mathbf{K}=\mathbf{I}=\begin{pmatrix}1.0 & 0.0\\ 0.0 & 1.0\end{pmatrix} \tag{6}$$

is simulated on a quadrilateral grid shown in Figure 9 (left), which has the exact solution $p=16x(1-x)y(1-y)$. Obviously, the two principal directions of the isotropic tensor (6) are parallel with the x- and y-axis as shown in Figure 3(b). However, they are not aligned with the quadrilateral grid directions. Hence, it is still a non-$\mathbf{K}$-orthogonal grid.

Figure 8 shows the comparison results of the convergence rate for the pressure and the normal velocity, it can be observed that the O-method still gives good results with $\mathcal{O}(h^2)$. The orders of the pressure and the normal velocity for the 'MPFA L: L+O' method are almost the same as those for the 'MPFA L: full O' method, which still show the superconvergence with $\mathcal{O}(h^{1.9})$ and $\mathcal{O}(h^{1.5})$, respectively; however, they are reduced. This can be explained by Figure 9 (right) and Figure 10 which show the local relative error for the normal velocity of the three numerical strategies. It is obvious that the O-method still exhibits small errors for the whole domain with the biggest magnitude 10^{-10}, whereas 'L+O' and 'full O' are both with the biggest magnitude 10^{-7}, which is larger than the O-method. Note that in this case, the 'full O' boundary discretization does not improve the error for the normal velocity due to the relatively big errors inside the domain where the grid has a bad behavior. Hence, the Dirichlet boundary influence can be ignored for this case compared with the interior errors. The reason for the occurrence of the big errors inside the domain for the L-method is described later in Section 3.4.

2.2.4. General quadrilateral grid with mild anisotropy. In fact, the above two numerical examples are special cases of the non-$\mathbf{K}$-orthogonal grid. The first example is tested on a very special grid, which aligns with the x- and y-axis but with a full tensor $\mathbf{K}$; and the second example is set up with a very special tensor, which aligns with the x- and y-axis but is solved on a non-orthogonal grid. For completeness, we also show the numerical example on a much more general quadrilateral grid with a general permeability tensor, see Figure 3(c). Hence, the simulation results of the same numerical

DOI: 10.1002/fld

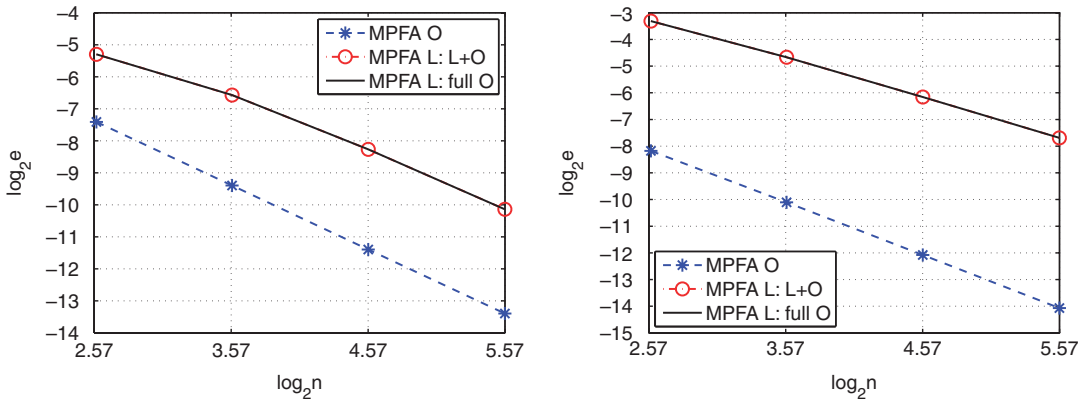

Figure 8. Convergence-order graph on quadrilateral grid: pressure (left), normal velocity (right).

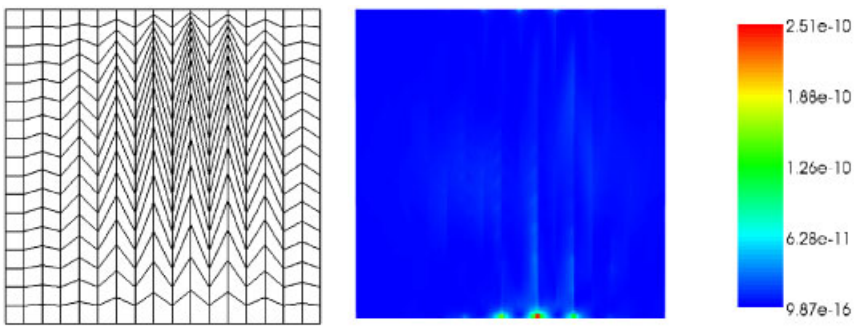

Figure 9. Quadrilateral grid (left, level 0), local relative error graph for normal velocity of O-method (right, level 3).

example on a general quadrilateral grid (see Figure 11 (left)) as the one on the rectangular grid are given in this subsubsection.

From Figure 11 (right) and Figure 12, it can be seen that in this general case, the O-method has the same magnitude 10^{-8} of the biggest error as the L-method with both boundary discretizations. Nevertheless, the L-method has bigger errors than the O-method in some local regions, where the grid has a bad behavior. Moreover, the boundary influence near the left-top corner of the domain occurring in the 'MPFA L: L+O' method is eliminated by applying the new boundary discretization 'full O', and the error values are also decreased. These observations are helpful to understand how the convergence-order graphs should look like.

As shown in Figure 13 (right), the convergence rate for the normal velocity of the 'MPFA L: L+O' method is $\mathcal{O}(h^{1.6})$ rather than $\mathcal{O}(h^2)$ for the O-method due to the big errors in some local regions. After using the improved boundary strategy 'full O', the convergence order is slightly increased to $\mathcal{O}(h^{1.7})$. As the above two numerical examples, the convergence behaviors of the

DOI: 10.1002/fld

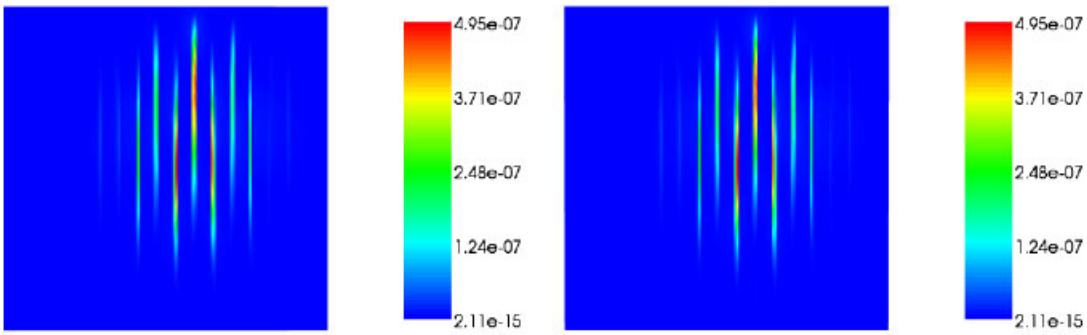

Figure 10. Local relative error graph for normal velocity of 'L-method: L+O' (left, level 3) and 'full O' (right, level 3).

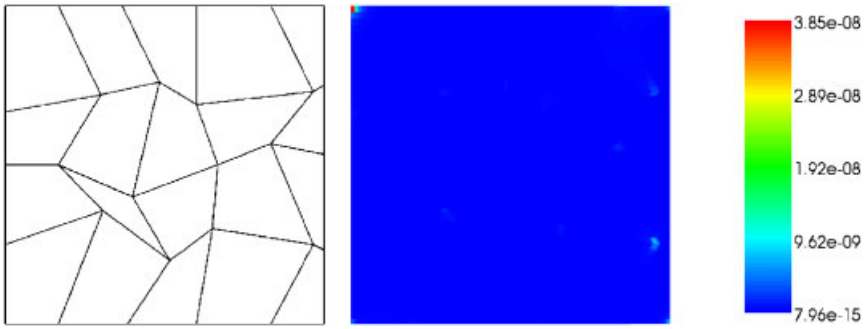

Figure 11. General quadrilateral grid (left, level 0), local relative error graph for normal velocity of O-method (right, level 4).

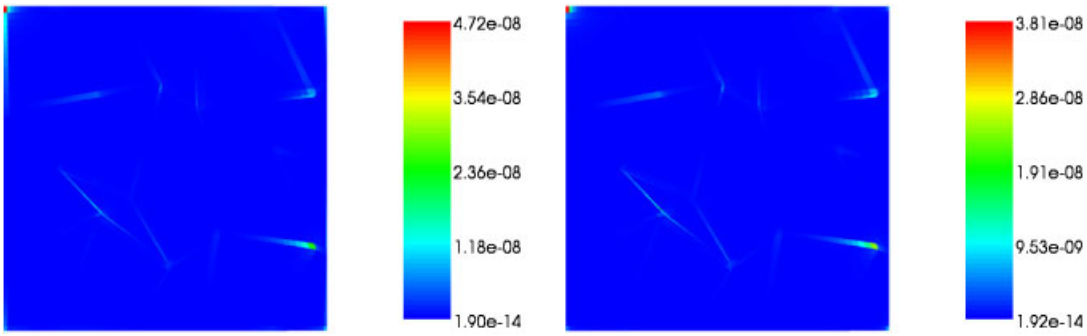

Figure 12. Local relative error graph for normal velocity of 'L-method: L+O' (left, level 4) and 'full O' (right, level 4).

DOI: 10.1002/fld

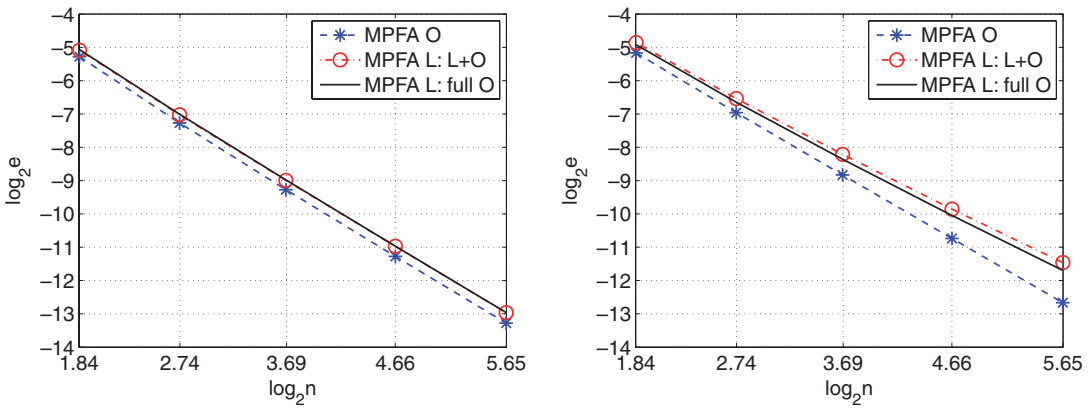

Figure 13. Convergence-order graph on general quadrilateral grid: pressure (left), normal velocity (right).

pressure are similar for all the three methods, which all achieve $\mathcal{O}(h^2)$ order as illustrated in Figure 13 (left).

In fact, the new method 'MPFA L: full O' is introduced here to improve the convergence of the normal velocity by reducing the boundary error. However, it cannot deal with the big errors coming from the shape of the grid. Therefore, the efficiency of the improvement differs from different grids. For some cases, the 'full O' strategy can completely recover the superconvergence order of the normal velocity, such as the numerical example shown in Section 2.2.2; for some cases, it does not make any sense since the boundary error is not the main contribution to the convergence behavior, see Section 2.2.3; for the other cases, it works in between, i.e. the convergence rate is increased somehow but not that much, refer to the general case in Section 2.2.4. As a conclusion, compared with the O-method, the superconvergence behavior of the L-method depends in a more sensitive way on the Dirichlet boundary handling and on the shape of the grid.

3. THE MPFA L-METHOD WITH HOMOGENEOUS MEDIA

Throughout this section, we assume that the tensor $\mathbf{K}$ is homogeneous in the computational domain Ω. All the theoretical results and explanations on the MPFA L-method here are discussed and given based on this assumption.

3.1. The simplified MPFA L-method

First, Lemma 3.1 is stated and proven to show that the implementation of the L-method can be significantly simplified for the homogeneous media.

Lemma 3.1

Under the assumption that $\mathbf{K}$ is homogeneous on Ω, the computation of the L-method described in Section 2.1(i) can be simplified as: the flux f through each half edge e (see Figure 14 (left)) is given as $f = -\mathbf{K}\nabla p \cdot \mathbf{n}_e$, where $\mathbf{n}_e$ is the scaled normal vector on e, having the same length as e; p is a linear pressure function uniquely given by the values at the three different cell centers

DOI: 10.1002/fld

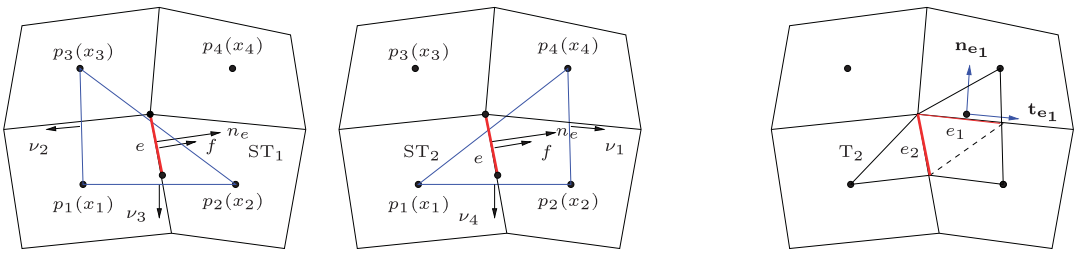

Figure 14. Simplified L triangle 1 (ST_1) and simplified L triangle 2 (ST_2) (left) for the simplified L-method, original L triangle 2 (T_2, right).

of either the simplified L triangle 1 or the simplified L triangle 2 in Figure 14 (left), which are in short denoted as ST_1 and ST_2, respectively; and

$$\nabla p = \begin{cases} -\dfrac{1}{2F_1}[(p_2-p_1)v_2+(p_3-p_1)v_3] & \mathrm{ST}_1 \text{ is chosen} \\ -\dfrac{1}{2F_2}[(p_1-p_2)v_1+(p_4-p_2)v_4] & \mathrm{ST}_2 \text{ is chosen} \end{cases}$$

Here, F_1 and F_2 are the areas of ST_1 and ST_2, v_i $(i=1,\ldots,4)$ are the normal vectors having the same lengths as the edges they are normal to.

Proof

It is enough to prove that the jump $[\nabla p]$ is zero on the half edge e_1 and e_2 of the original L triangle T_2 in Figure 14 (right). As shown in the figure, $\mathbf{n}_{e_1}$ and $\mathbf{t}_{e_1}$ are the unit normal and tangential vectors of e_1. Since the L-method requires full pressure continuity and flux continuity on e_1, and $\mathbf{K}$ is symmetric and homogeneous on Ω, hence

$$[\nabla p\cdot\mathbf{t}_{e_1}]=0, \quad [\mathbf{K}\nabla p\cdot\mathbf{n}_{e_1}]=[\nabla p\cdot\mathbf{K}^{\mathrm{T}}\mathbf{n}_{e_1}]=[\nabla p\cdot\mathbf{K}\mathbf{n}_{e_1}]=0 \tag{7}$$

Using the fact that $\mathbf{K}$ is positive definite, it is easy to see that $\mathbf{t}_{e_1}$ and $\mathbf{K}\mathbf{n}_{e_1}$ are independent, thus $[\nabla p]|_{e_1}=0$. Similarly, we have $[\nabla p]|_{e_2}=0$. Hence, ∇p is constant on T_2 and the desired result follows. □

3.2. The explanation on the criterion for choosing the L triangle

In this subsection, the criterion for choosing the L triangle introduced in [17] is reinterpreted in a more intuitive way. An equivalent criterion is put forward, which yields more insight into the L-method.

Note that the two choices of the L triangle related to the half edge $\overline{\bar{x}_1\bar{x}_3}$ in Figure 1 are T_1 and T_2, and $\mathbf{n}_e$ denotes the scaled normal vector on the half edge $\overline{\bar{x}_1\bar{x}_3}$, having the same length as $\overline{\bar{x}_1\bar{x}_3}$. From Lemma 3.1, it is obvious that the flux f through the half edge $\overline{\bar{x}_1\bar{x}_3}$ can be calculated by the simplified L triangle shown in Figure 14 (left), either ST_1 or ST_2, which are $\triangle x_1x_2x_3$ or $\triangle x_1x_2x_4$, respectively.

Given $\mathrm{ST}_1, \mathrm{ST}_2$ and $\mathbf{K}^{\mathrm{T}}\mathbf{n}_e$, as shown in Figure 15, we can draw the line segment $\overline{x_1x_1'}$ through the point x_1 along the direction of $\mathbf{K}^{\mathrm{T}}\mathbf{n}_e$, which intersects with the edge $\overline{x_2x_3}$ at the point x_1' and

DOI: 10.1002/fld

has the length l_1. Similarly, the line segment $\overline{x_2x_2'}$ is drawn along the direction of $\mathbf{K}^{\mathrm{T}}\mathbf{n}_e$ with the length l_2. Here, the pressure values at the point x_1' and x_2' are denoted as p_1' and p_2', respectively.

Lemma 3.2
Let the expressions of the flux f through the half edge $\overline{\bar{x}_1\bar{x}_3}$ calculated from both L triangles (T_1 and T_2 or ST_1 and ST_2) be

$$f=\begin{cases} t_1^1 p_1+t_2^1 p_2+t_3^1 p_3 & \text{from } \mathrm{T}_1 \text{ or } \mathrm{ST}_1 \\ t_1^2 p_1+t_2^2 p_2+t_4^2 p_4 & \text{from } \mathrm{T}_2 \text{ or } \mathrm{ST}_2 \end{cases} \tag{8}$$

as described in the first step (i) of the L-method in Section 2.1. Then the criterion originally introduced in [17] for choosing the proper L triangle

$$\begin{cases} \text{if } |t_1^1|<|t_2^2| & \text{choose } \mathrm{T}_1 \\ \text{otherwise} & \text{choose } \mathrm{T}_2 \end{cases} \tag{9}$$

is equivalent to the following criterion:

$$\begin{cases} \text{if } l_1>l_2 & \text{choose } \mathrm{T}_1 \text{ or } \mathrm{ST}_1 \\ \text{otherwise} & \text{choose } \mathrm{T}_2 \text{ or } \mathrm{ST}_2 \end{cases} \tag{10}$$

Proof
From (8), we have

$$-\mathbf{K}\nabla p\cdot\mathbf{n}_e=\begin{cases} t_1^1 p_1+t_2^1 p_2+t_3^1 p_3 & \text{from } \mathrm{T}_1 \text{ or } \mathrm{ST}_1 \\ t_1^2 p_1+t_2^2 p_2+t_4^2 p_4 & \text{from } \mathrm{T}_2 \text{ or } \mathrm{ST}_2 \end{cases} \tag{11}$$

On the other hand, in terms of the construction of $\overline{x_1x_1'}$ and $\overline{x_2x_2'}$, we let

$$x_1-x_1'=\alpha_1\mathbf{K}^{\mathrm{T}}\mathbf{n}_e, \quad x_2-x_2'=\alpha_2\mathbf{K}^{\mathrm{T}}\mathbf{n}_e$$

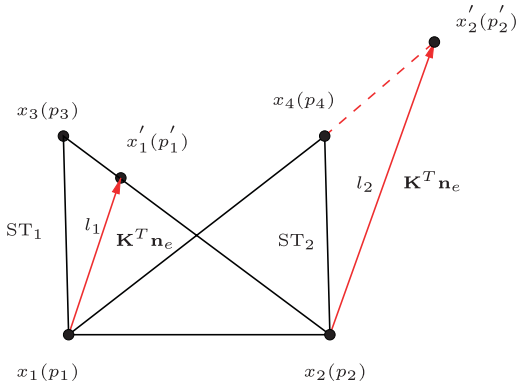

Figure 15. Explanation on the criterion for choosing the L triangle.

DOI: 10.1002/fld

where α_1 and α_2 are two constant scaling factors. Thus,

$$l_1 = |\alpha_1||\mathbf{K}^{\mathrm{T}}\mathbf{n}_e|, \quad l_2 = |\alpha_2||\mathbf{K}^{\mathrm{T}}\mathbf{n}_e| \tag{12}$$

Since $\nabla p \cdot \mathbf{K}^{\mathrm{T}}\mathbf{n}_e$ is the gradient of p along the direction of $\mathbf{K}^{\mathrm{T}}\mathbf{n}_e$, we have

$$-\mathbf{K}\nabla p \cdot \mathbf{n}_e = -\nabla p \cdot \mathbf{K}^{\mathrm{T}}\mathbf{n}_e = \begin{cases} \dfrac{p_1' - p_1}{\alpha_1 |\mathbf{K}^{\mathrm{T}}\mathbf{n}_e|} & \text{from } \mathrm{ST}_1 \\ \dfrac{p_2' - p_2}{\alpha_2 |\mathbf{K}^{\mathrm{T}}\mathbf{n}_e|} & \text{from } \mathrm{ST}_2 \end{cases} \tag{13}$$

Note that in Figure 15, p_1' only depends on p_2 and p_3, and p_2' only depends on p_1 and p_4 according to Lemma 3.1, so comparing (11) with (13) we obtain

$$t_1^1 = -\frac{1}{\alpha_1 |\mathbf{K}^{\mathrm{T}}\mathbf{n}_e|}, \quad t_2^2 = -\frac{1}{\alpha_2 |\mathbf{K}^{\mathrm{T}}\mathbf{n}_e|}$$

Combining with (12), it is easy to obtain

$$|t_1^1| = \frac{1}{l_1}, \quad |t_2^2| = \frac{1}{l_2} \tag{14}$$

From (14), it is obvious that the criterion (9) is equivalent to the criterion (10), which gives an intuitive description of the original principle for choosing the L triangle. □

Remark

Lemma 3.2 is derived only for the special case with homogeneous media, and it is difficult to abstract the equivalent criterion for the heterogeneous case due to the different $\mathbf{K}$ values for the two choices of the L triangle. Nevertheless, the same principle should work for the general case with heterogeneous permeability tensor.

Based on Lemma 3.2, the choice range of two L triangles is illustrated below from two points of view, and the two picture descriptions are useful and explicit for getting a good understanding of the L-method.

3.2.1. Illustration 1. We start by assuming that the simplified L triangle ST_1 for a half edge e and the vector $\mathbf{K}^{\mathrm{T}}\mathbf{n}_e$ with length l_1 are given as shown in Figure 16. Now we want to find out in which part of the plane the center point x_4 can be placed, such that the simplified L triangle ST_1 is chosen in terms of the criterion (9); in the other part, the L triangle ST_2 formed by points x_1, x_2 and x_4 is chosen. Here, $\mathbf{n}_e$ is the scaled normal vector on e as defined before, $x_i, i = 1, \ldots, 4$ are the cell centers.

Referring to the equivalence between criterion (9) and (10) in Lemma 3.2, we can simply draw a line segment with the length l_1 starting from the point x_2 in the direction of the vector $\mathbf{K}^{\mathrm{T}}\mathbf{n}_e$, which ends at the point x_2', see Figure 17. In a similar way but in the opposite direction of $\mathbf{K}^{\mathrm{T}}\mathbf{n}_e$, the line segment $\overline{x_2 x_2''}$ is drawn. Finally, the straight line through points x_1, x_2' and another line

DOI: 10.1002/fld

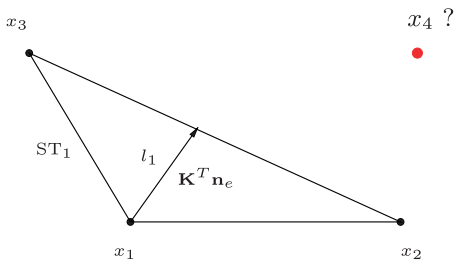

Figure 16. Given the simplified L triangle ST_1 and the vector $\mathbf{K}^{\mathrm{T}}\mathbf{n}_e$.

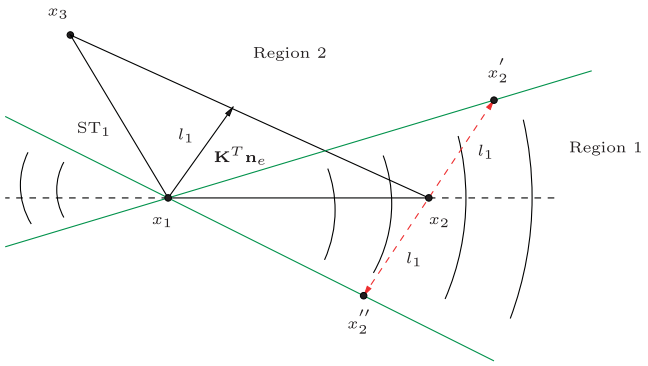

Figure 17. The two regions for the unknown point x_4.

through points x_1, x_2'' can be determined. Here, the shadowed region bounded by the lines $\overline{x_1x_2'}$ and $\overline{x_1x_2''}$ is denoted as Region 1, which excludes $\overline{x_1x_2'}$ and $\overline{x_1x_2''}$, and the remaining part is Region 2. Obviously, according to the equivalent criterion (10), we have

$$\text{point } x_4 \text{ locates in } \begin{cases} \text{Region 1:} & l_1 > l_2 & \text{choose L triangle } \mathrm{ST}_1 \\ \text{Region 2:} & l_1 \leqslant l_2 & \text{choose L triangle } \mathrm{ST}_2 \end{cases} \tag{15}$$

Remark

Actually, for the L-method, it is only possible for the point x_4 to be on the same side as the point x_3, i.e. above the straight line $\overline{x_1x_2}$ in Figure 17. Therefore, (15) can be rewritten as

$$\text{point } x_4 \text{ locates in } \begin{cases} \text{Region 1 above } \overline{x_1x_2}: & l_1 > l_2 & \text{choose L triangle } \mathrm{ST}_1 \\ \text{Region 2 above } \overline{x_1x_2}: & l_1 \leqslant l_2 & \text{choose L triangle } \mathrm{ST}_2 \end{cases} \tag{16}$$

3.2.2. Illustration 2. Given the simplified L triangles ST_1 and ST_2 for a half edge e as shown in Figure 18, we want to find out two direction ranges of the vector $\mathbf{K}^{\mathrm{T}}\mathbf{n}_e$. In one range, the L triangle ST_1 is chosen, and in the other range, the L triangle ST_2 is chosen. Here, $\mathbf{n}_e$ is the scaled normal vector on e as defined before, $x_i, i = 1, \ldots, 4$ are the cell centers.

DOI: 10.1002/fld

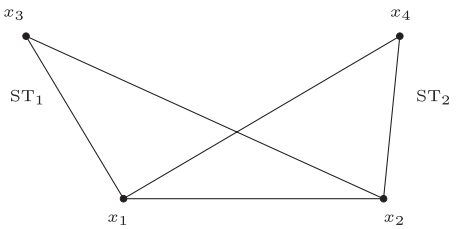

Figure 18. Given the simplified L triangles ST_1 and ST_2.

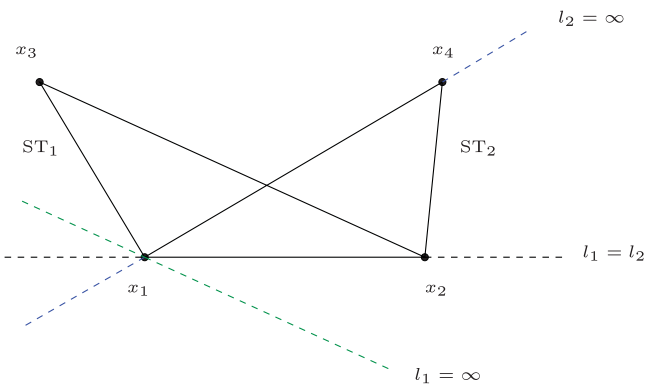

Figure 19. Three critical lines for the direction of $\mathbf{K}^{\mathrm{T}}\mathbf{n}_e$.

Applying the equivalent criterion (10), the direction regions of $\mathbf{K}^{\mathrm{T}}\mathbf{n}_e$ can be obtained in three steps as illustrated in Figures 19–21:

(1) Initially, it is obvious to observe three critical directions for the vector $\mathbf{K}^{\mathrm{T}}\mathbf{n}_e$ as shown in Figure 19: (i) the straight line through the points x_1 and x_2 along which we have $l_1 = l_2$; (ii) the line connecting x_1 and x_4 with $l_2 = \infty$; (iii) the straight line through the point x_1 in parallel with the line segment $\overline{x_2x_3}$. Along this direction, $l_1 = \infty$.

(2) Although the above three critical lines have been found, there is still one more with the relation $l_1 = l_2$ missing. To search for it, a parallelogram is constructed as given in Figure 20. Based on the intersection triangle $\triangle x_1x_2x_c$ of ST_1 and ST_2, a parallelogram $x_1x_2x_2'x_1'$ can be easily constructed using the length of $\overline{x_1x_c}$ and $\overline{x_2x_c}$. Obviously, the line segments $\overline{x_1x_1'}$ and $\overline{x_2x_2'}$ are parallel and have the same length. Thus, if the direction of $\mathbf{K}^{\mathrm{T}}\mathbf{n}_e$ is along the line $\overline{x_1x_1'}$, then $l_1 = l_2$, which gives the fourth critical line.

(3) Combining steps (1) and (2) in one figure, we find all four straight lines with critical directions for $\mathbf{K}^{\mathrm{T}}\mathbf{n}_e$. From Figure 21, it is easy to conclude that

$$\text{the direction of } \mathbf{K}^{\mathrm{T}}\mathbf{n}_e \text{ is in } \begin{cases} \text{Region 1:} & l_1 > l_2 & \text{choose L triangle } ST_1 \\ \text{Region 2:} & l_1 \leqslant l_2 & \text{choose L triangle } ST_2 \end{cases} \tag{17}$$

DOI: 10.1002/fld

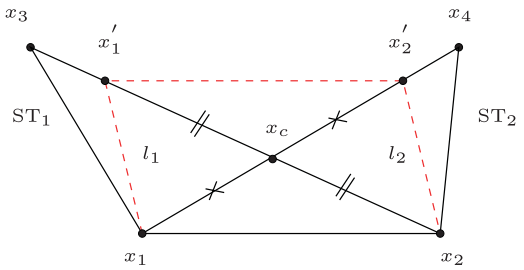

Figure 20. A parallelogram to search for the fourth critical direction.

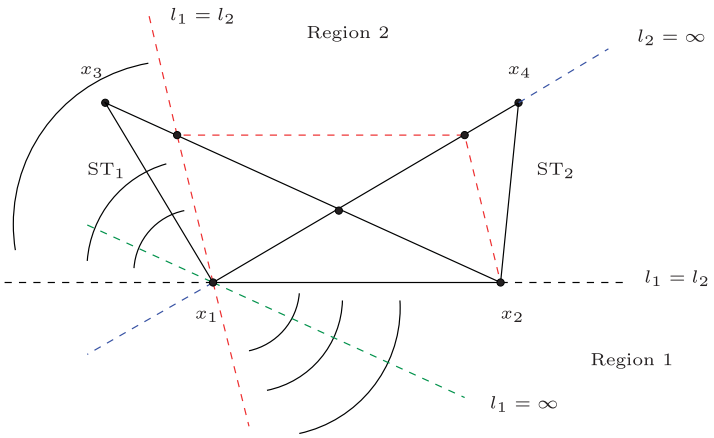

Figure 21. Two choice regions for the direction of $\mathbf{K}^{\mathrm{T}}\mathbf{n}_e$.

3.3. The combination of the two L triangles for an entire cell edge

Theorem 3.1

As shown in Figure 22, $x_i, i=1,\ldots,6$, are the cell centers. $\triangle x_1x_2x_3$ and $\triangle x_1x_2x_4$ in the right picture are the two simplified L triangles corresponding to the first half edge e_1 of one cell edge, which are shortly denoted as ST_1 and ST_2, respectively. $\triangle x_1x_2x_5$ and $\triangle x_1x_2x_6$ are the two simplified L triangles corresponding to the second half edge e_2 of the cell edge, which are shortly denoted as ST_4 and ST_3, respectively. If the polygon constructed by the points $x_i, i=1,\ldots,6$, is a parallelogram, i.e. it can be expressed as $x_3x_4x_6x_5$, then

(1) the combination choice of the two simplified L triangles for e_1 and e_2 is either $(\mathrm{ST}_1, \mathrm{ST}_3)$ or $(\mathrm{ST}_2, \mathrm{ST}_4)$;
(2) correspondingly, the choice of the two original L triangles shown in Figure 22 (left) for e_1 and e_2 is either $(\mathrm{T}_1, \mathrm{T}_3)$ or $(\mathrm{T}_2, \mathrm{T}_4)$.

Proof

(1) We show that if ST_1 is taken, then the choice ST_4 is impossible, and if ST_2 is selected, then ST_3 is impossible. Referring to the Illustration 2 for the region for the direction of $\mathbf{K}^{\mathrm{T}}\mathbf{n}_e$ in Figure 21,

DOI: 10.1002/fld

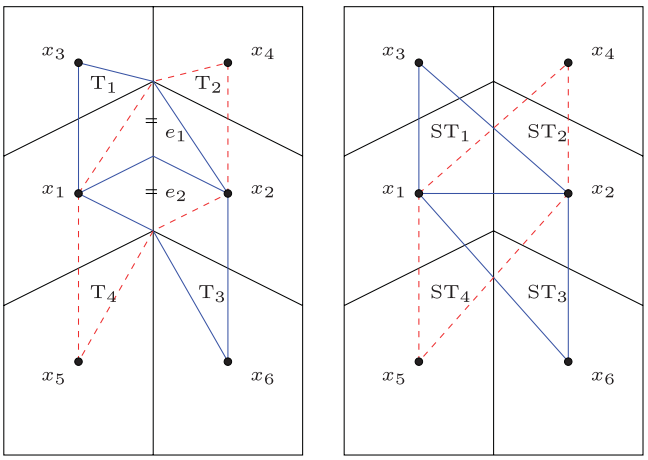

Figure 22. Four L triangles for a cell edge: original L (left), simplified L (right).

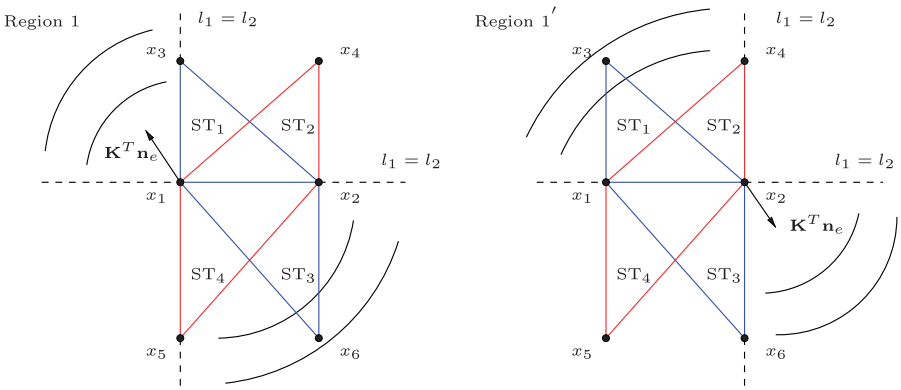

Figure 23. Direction region of $\mathbf{K}^{\mathrm{T}}\mathbf{n}_e$ for choosing: ST_1 (left), ST_3 (right).

it is easy to find Region 1 for $\mathbf{K}^{\mathrm{T}}\mathbf{n}_e$ in which the simplified L triangle ST_1 is chosen for the first half edge e_1 as shown in Figure 23 (left). Similarly, Region $1'$ is obtained for the second half edge e_2 in which ST_3 is chosen, see Figure 23 (right). Since the polygon constructed by the points $x_i, i=1,\ldots,6$, is a parallelogram; hence, the line through the points x_3 and x_5 is parallel with the one through points x_4 and x_6. Therefore, Region 1 is the same as Region $1'$. In other words, if the vector $\mathbf{K}^{\mathrm{T}}\mathbf{n}_e$ points in the direction within Region 1, then the combination (ST_1, ST_3) is chosen for the entire cell edge in terms of the original criterion (9); in the rest of the plane, the combination (ST_2, ST_4) is used to calculate the flux.

(2) It follows from the above result and Lemma 3.1. □

Corollary 3.1 (*Extension of Theorem 3.1*)
As seen from Figure 24, $\triangle x_1x_2x_3$ and $\triangle x_1x_2x_4$ are the two simplified L triangles corresponding to the first half edge e_1 of one cell edge, which are shortly denoted as ST_1 and ST_2, respectively.

DOI: 10.1002/fld

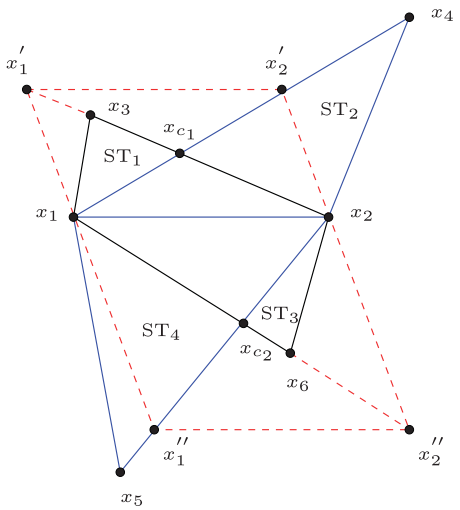

Figure 24. Four simplified L triangles with two constructed parallelograms.

$\triangle x_1x_2x_5$ and $\triangle x_1x_2x_6$ are the two simplified L triangles corresponding to the second half edge e_2 of the cell edge, which are shortly denoted as ST_4 and ST_3, respectively. Obviously, $\triangle x_1x_2x_{c_1}$ is the intersection triangle of ST_1 and ST_2, and $\triangle x_1x_2x_{c_2}$ is the intersection triangle of ST_3 and ST_4. Using these two intersection triangles, one can construct two parallelograms $x_1x_2x_2'x_1'$ and $x_1x_2x_2''x_1''$ in the same way as described in Figure 20. If the two artificial parallelograms can form a whole parallelogram $x_1'x_2'x_2''x_1''$ as shown in Figure 24, then the two conclusions in Theorem 3.1 also hold.

Corollary 3.2
In Figure 25 (left), given the simplified L triangles ST_1 ($\triangle x_1x_2x_3$) and ST_2 ($\triangle x_1x_2x_4$) for the first half edge e_1 of one cell edge, and ST_3 ($\triangle x_1x_2x_6$) and ST_4 ($\triangle x_1x_2x_5$) for the second half edge e_2. Parallelograms $x_1x_2x_2'x_1'$ and $x_1x_2x_2''x_1''$ are constructed by the intersection triangle $\triangle x_1x_2x_{c_1}$ and $\triangle x_1x_2x_{c_2}$, respectively. When the two artificial parallelograms cannot form a whole parallelogram as shown in Figure 25, then there exists a region in which if the vector $\mathbf{K}^{\mathrm{T}}\mathbf{n}_e$ locates, the combination choice of the two simplified L triangles for e_1 and e_2 is either (ST_1, ST_4) or (ST_2, ST_3).

Proof
It can be easily proven by referring to Illustration 2 of the criterion in Figure 21. As shown in Figure 25 (right), the critical lines with $l_1 = l_2$ have been found for e_1 and e_2. Based on this, the shadowed region is obtained in which if $\mathbf{K}^{\mathrm{T}}\mathbf{n}_e$ locates, the choice of the simplified L triangle for e_1 is ST_2, whereas for e_2, ST_3 is chosen. That is, the choice of the simplified L triangles for the cell edge here is the combination (ST_2, ST_3). □

Remark
From Theorem 3.1, Corollaries 3.1 and 3.2, it can be concluded that in the case of homogeneous media, for uniform grids, the choice of the simplified L triangles for one cell edge is always the

DOI: 10.1002/fld

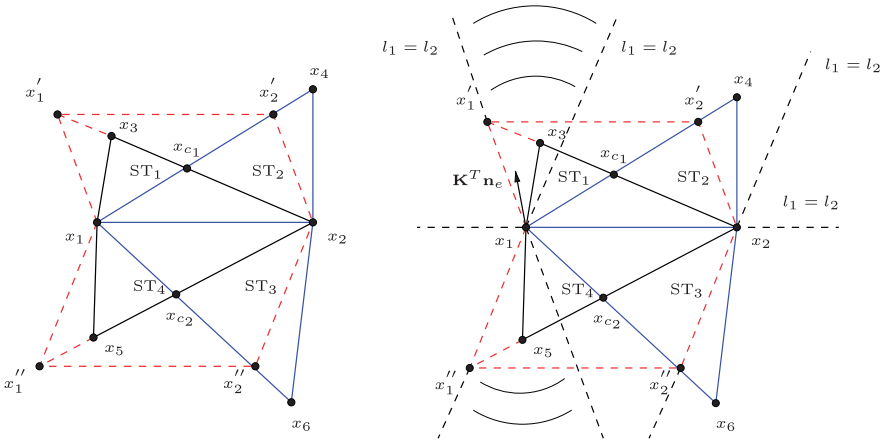

Figure 25. Example for choosing the combination $(\mathrm{ST}_2, \mathrm{ST}_3)$.

combination $(\mathrm{ST}_1, \mathrm{ST}_3)$ or $(\mathrm{ST}_2, \mathrm{ST}_4)$; but for distorted grids, it depends on the shape of the grid and the permeability tensor $\mathbf{K}$.

3.4. Discussion

Now, let us reconsider the numerical results of the problem in Section 2.2.3 with the isotropic, homogeneous $\mathbf{K}$ (6). Based on the above theoretical results and explanations on the L-method, under the assumption of a homogeneous permeability tensor, we will interpret why there are some big errors for the normal velocity appearing in the interior domain as shown in Figure 10.

Figure 26 shows part of the quadrilateral grid in Figure 9 (left) with bad behavior. Here, $x_i, i = 1, \ldots, 10$, are the cell centers, and $\bar{x}_j$, $j = 1, \ldots, 5$, are the cell nodes. Since $\mathbf{K}$ is homogeneous in this case; hence, all the theoretical results proposed in Section 3 can be applied for our discussion here.

According to Lemma 3.1, the flux through each cell edge can be equivalently calculated by the simplified L triangles. Thus, we intend to find out the two proper simplified L triangles for the calculation of the fluxes through the cell edge $\overline{\bar{x}_1\bar{x}_2}$ and $\overline{\bar{x}_4\bar{x}_5}$. Note that $\mathbf{K}$ is an identity matrix, so $\mathbf{K}^{\mathrm{T}}\mathbf{n}_e = \mathbf{n}_e$, where $\mathbf{n}_e$ is the scaled normal vector on a cell edge e. Therefore, it is easy to draw the vector $\mathbf{K}^{\mathrm{T}}\mathbf{n}_e$ of $\overline{\bar{x}_1\bar{x}_2}$ and $\overline{\bar{x}_4\bar{x}_5}$, see Figure 26.

First, for the cell edge $\overline{\bar{x}_1\bar{x}_2}$, since the direction of its $\mathbf{K}^{\mathrm{T}}\mathbf{n}_e$ is parallel with the critical line $\overline{x_1x_2}$ along which $l_1 = l_2$; hence, the combination $(\mathrm{ST}_2, \mathrm{ST}_4)$ is chosen in terms of the equivalent criterion (10), i.e. $(\triangle x_1x_2x_4, \triangle x_1x_2x_5)$. It can be observed that the quadrilateral $x_1x_4x_2x_5$ used for calculating the flux only covers the cell edge $\overline{\bar{x}_2\bar{x}_3}$ instead of $\overline{\bar{x}_1\bar{x}_2}$, which causes the 'information shift' for the flux calculation, and thus big errors on these parts of the grid occur.

For the cell edge $\overline{\bar{x}_4\bar{x}_5}$, it can be seen that the vector $\mathbf{K}^{\mathrm{T}}\mathbf{n}_e$ locates in Region 1 for both half edges of $\overline{\bar{x}_4\bar{x}_5}$. Hence, the combination of the two simplified L triangles for $\overline{\bar{x}_4\bar{x}_5}$ is $(\mathrm{ST}_1, \mathrm{ST}_3)$ according to (17), i.e. $(\triangle x_7x_8x_1, \triangle x_7x_8x_{10})$. Notice that the quadrilateral $x_7x_1x_8x_{10}$ symmetrically covers the inner part of the cell edge $\overline{\bar{x}_4\bar{x}_5}$, thus it can well provide the data information for the flux calculation. Obviously, the phenomenon of 'information shift' does not occur in this case.

From the above discussion and analysis for the two different kinds of cell edges, it can be expected that the big errors only appear in the vertical direction of the bad-behavior grid part. This is confirmed by our numerical experiments, see Figure 10.

DOI: 10.1002/fld

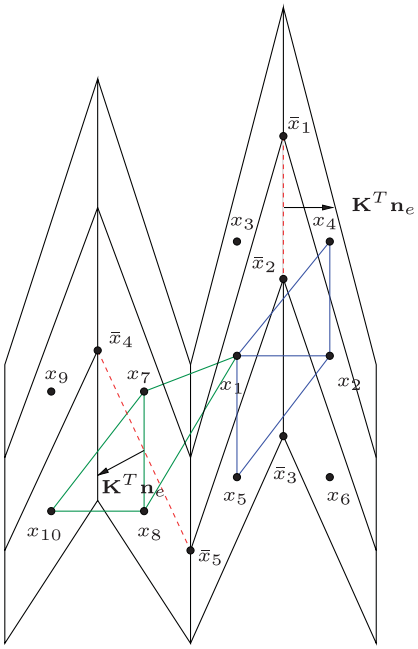

Figure 26. Part of the quadrilateral grid in Figure 9 (left) with bad behavior.

Remarks

As mentioned in [17], the L-method was developed to improve the monotonicity of the O-method on challenging grids and/or strong medium anisotropy. For severe grid aspect ratios and rough grid perturbations, large oscillations may occur in the pressure for the O-method, which can deteriorate its convergence behavior. The results in Section 2 show that the L-method performs not so good as the O-method in the aspect of convergence rate, such as for the example in Section 2.2.3. However, these two observations are not contradictory. First of all, the grid in Figure 9 (left) only has a moderate grid aspect ratio without the rough grid perturbation, and in this case only small oscillations may be seen for the O-method even if its monotonicity is violated, see [17]. Thus, the monotonicity may not affect the convergence rate of the O-method; in other words, both methods have almost the same competence for the monotonicity. Second, a large domain of monotonicity does not necessarily lead to a high convergence rate. For the grid in Figure 9 (left), the 'information shift' for the flux calculation mentioned above acts as a more important role for the convergence rate of the L-method compared with the monotonicity for the O-method. Therefore, the grid shape and the permeability tensor can influence the convergence rate of both methods but from different points of view, i.e. the monotonicity for the O-method and the choice of the L triangles for the L-method.

Although the monotonicity of the L-method is improved compared with the O-method as shown in [17], the convergence rate for the L-method can be worse than for the O-method. This fact can be explained by the observed 'information shift' illustrated in Figure 26. Notice that regardless of the combination of the L triangles that is chosen, the 'information shift' will always exist, which becomes a weak point of the L-method. In other words, it does not depend on the criterion for

DOI: 10.1002/fld

choosing the L triangles but on the shape of the grid. There might be several possibilities to alleviate the problem such as: (i) grid adaptivity and (ii) the moving node method. Both possibilities first check if the quality of the grid is good enough for the implementation of the L-method before computation, then (i) performs the grid refinement to improve the grid behavior while (ii) changes the local grid shape by moving the existing nodes. (iii) The third possibility is to use a fictitious grid in the local region where the grid behavior is bad for the more exact calculation of the flux. All the remedies we can think of so far are rather artificial and might work in one special case but not in the next one.

4. THE MPFA L-METHOD FOR TWO-PHASE FLOW

In this section, the MPFA L-method is applied to simulate a simplified two-phase flow model—the Buckley–Leverett (BL) problem in porous media on general quadrilateral grids. Here, only the 'L+O' boundary strategy is implemented. Numerical results using the L-method are given for both the pressure and the saturation and are also compared with the simulation results using the TPFA. In order to apply the L-method, the fractional flow formulation (18) and (19) of the BL problem is chosen for the implementation, which is derived in [1]:

$$\nabla \cdot \mathbf{v}_t = 0, \quad \mathbf{v}_t = -\lambda_t \mathbf{K} \nabla \bar{p} = -\lambda_t \mathbf{K} \nabla p_w \tag{18}$$

$$\phi \frac{\partial S_w}{\partial t} + \nabla \cdot (f_w(S_w)\mathbf{v}_t) = 0 \tag{19}$$

Here, ϕ is the porosity, $\mathbf{K}$ the intrinsic permeability, $\lambda_\alpha = k_{r\alpha}/\mu_\alpha$ is the *mobility* of phase α, $\alpha \in \{w, n\}$, where $k_{r\alpha}$ is the relative permeability, μ_α the dynamic viscosity. S_w and p_w are the saturation and the pressure of wetting phase; $\mathbf{v}_t$ the *total velocity*, $\lambda_t = \sum_\alpha \lambda_\alpha$ is the *total mobility*; *fractional flow function* f_α is denoted by $f_\alpha = \lambda_\alpha/\lambda_t$. Notice that the pressure equation (18) has the same elliptic operator as in the model equation (1), hence, the MPFA L-method described in Section 2.1 can be directly applied to the above simplified two-phase flow problem.

Both Equations (18) and (19) are only weakly coupled through the relative permeability in the pressure equation (18). Therefore, the system can be solved sequentially by the IMplicit-Pressure-Explicit-Saturation method (IMPES), see [1], i.e. the pressure equation (18) is first solved implicitly using the MPFA L-method, then the saturation equation (19) is solved explicitly using the velocity field derived from the pressure equation. For the detailed MPFA L-discretization scheme of (18), refer to the short description in Section 2.1 and [17]. Furthermore, the pressure values obtained from the pressure equation (18) are used to compute the total velocity for the saturation equation by reusing the MPFA L-method, i.e. to derive the total velocity field through the flux expression for each half cell edge as shown in (8).

For the saturation equation (19), let $\mathcal{J} = \{t^0, t^1, \ldots, t^M\}$ be a partition of the time interval $[0, T]$ and $\triangle t^n = t^{n+1} - t^n$ is the time step. Based on the total velocity field derived from the pressure equation, an upwind CCFV scheme using the TPFA method is defined for the saturation equation over each cell ω_i as:

$$S_{wi}^{n+1} = S_{wi}^n - \frac{\triangle t^n}{\phi} \sum_{\gamma_{ij}} \frac{|\gamma_{ij}|}{|\omega_i|} (f_w(S_{wi}^n) \max(0, \mathbf{v}_{tij}^n \cdot \nu_{ij}) + f_w(S_{wj}^n) \max(0, -\mathbf{v}_{tij}^n \cdot \nu_{ij})) \tag{20}$$

DOI: 10.1002/fld

Here, S_{wi}^n denotes the saturation of the wetting phase in the cell center of ω_i at time t^n, the cell boundary $\partial\omega_i$ is divided into four facets, γ_{ij}. $|\gamma_{ij}|$ and $|\omega_i|$ denote the measure of γ_{ij} and ω_i, respectively, $\mathbf{v}_{tij}^n$ is the total velocity on γ_{ij} at time t^n, v_{ij} is the unit outer normal of γ_{ij}. On an inflow facet γ_{ij}, we formally set $S_{wj}^n = J(\gamma_{ij})$, where $J(\gamma_{ij})$ is the Neumann boundary value on γ_{ij}. The Courant–Friedrichs–Lewy criterion is applied to determine the time step in the simulation since the IMPES method is only conditionally stable due to the explicit numerical scheme (20) for the saturation equation. It should be mentioned that the numerical experiments using the TPFA method are performed as follows: first, solve the pressure equation by the TPFA method, then reuse the TPFA method to get the total velocity field, and finally solve the saturation equation using the same upwind scheme as (20).

The BL problem describes an instationary displacement of a non-wetting phase by a wetting phase in a quasi-one-dimensional, horizontal domain. Boundary and initial conditions are depicted in Figure 27. Here, $\mathbf{K} = k\mathbf{I}, k = 10^{-10}, \mathbf{I}$ is the identity matrix. $\mu_w = \mu_n = 0.001(\mathrm{mPas})$, $\phi = 0.2$ and the nonlinear Brooks–Corey k_r–S_w relation is used.

In the following, all the simulation results are given at time $t = 1.0 \times 10^7$ s. Here, the numerical results on a very fine rectangular grid (see Figure 28 (left)) are computed as the reference solutions for the pressure and saturation as shown in Figure 29. The discretization scheme for obtaining the reference solutions can be either the TPFA method or the MPFA L-method since in this case the MPFA L-method reduces to the TPFA method.

The numerical experiment using the MPFA L-method is first tested on the grid in Figure 28 (right), and is compared with the results of the TPFA method. Figures 30 and 31 show the pressure and saturation contour for the TPFA method and the MPFA L-method, respectively. The four graphs are the results calculated on the grid after two refinements of Figure 28 (right). Obviously,

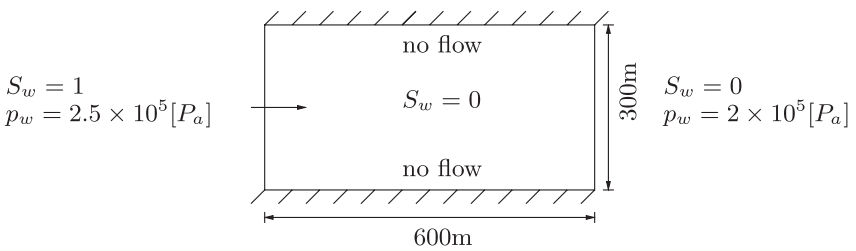

Figure 27. Boundary and initial conditions for Buckley–Leverett problem.

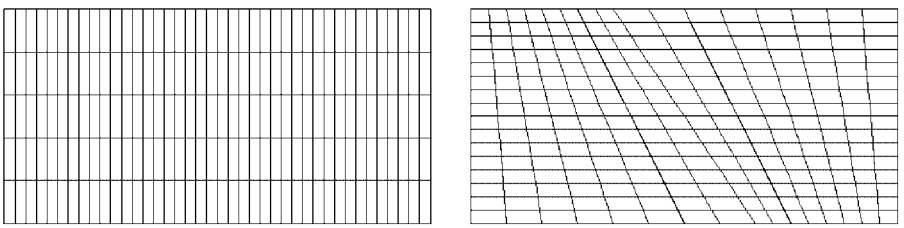

Figure 28. Rectangular grid (left) and general quadrilateral grid (right, level 3).

DOI: 10.1002/fld

Figure 29. Reference solutions for pressure (left) and saturation (right).

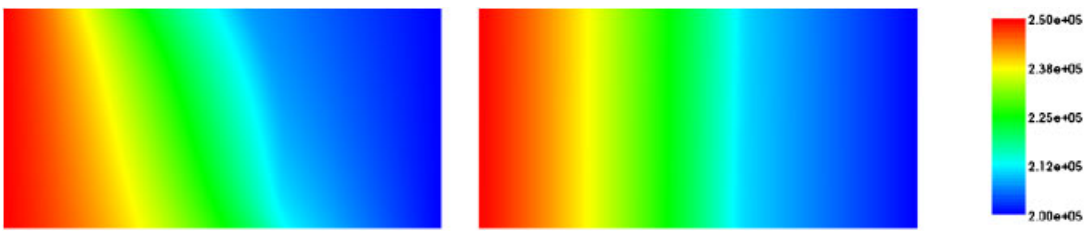

Figure 30. Pressure contour for TPFA method (left) and MPFA L-method (right).

Figure 31. Saturation contour for TPFA method (left) and MPFA L-method (right).

the saturation for the TPFA method (see Figure 31 (left)) exhibits more smearing in comparison with the reference solution in Figure 29 (right), and the saturation front is wrong due to the distorted pressure shown in Figure 30 (left), which is affected by the shape of the grid. From Figures 30 (right) and 31 (right), we can see that the MPFA L-method converges well to the reference solutions.

Next, the grid in Figure 32 (right) is applied for the simulation, which is derived by refining the grid in Figure 32 (left) twice. From the left coarse grid, it is observed that the grid behavior is very bad in some local regions, where its aspect ratios are quite large. The results in Figures 33 and 34 are the pressure and saturation contour for the TPFA method and the MPFA L-method, respectively. It is clear that the convergence of the TPFA method is completely lost in this case,

DOI: 10.1002/fld

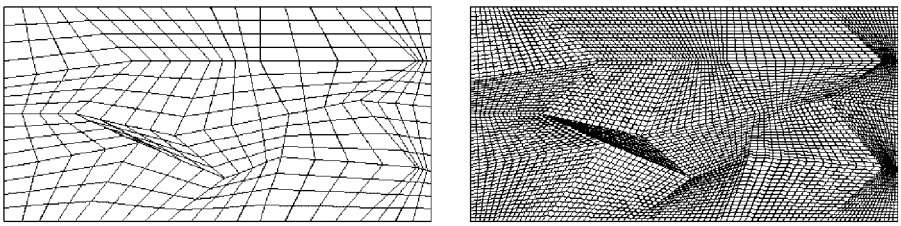

Figure 32. General quadrilateral grid: level 2 (left), level 4 (right).

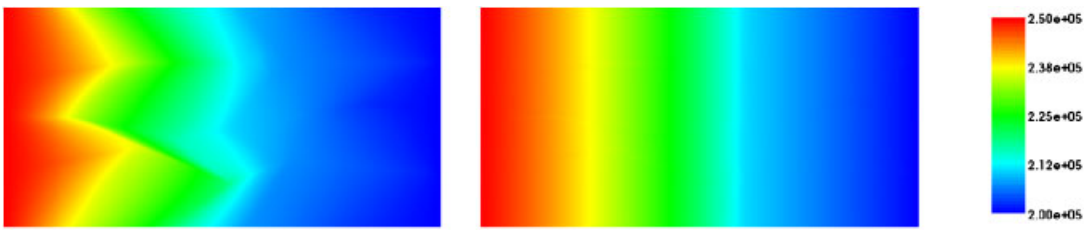

Figure 33. Pressure contour for TPFA method (left) and MPFA L-method (right).

Figure 34. Saturation contour for TPFA method (left) and MPFA L-method (right).

and the solutions are much worse than those computed on the grid in Figure 28 (right). Instead, the MPFA L-method still works well, but compared with the test on the grid in Figure 28 (right), the solutions here converge for a smaller grid size. That means the convergence rate of the MPFA L-method is reduced in this case, which coincides with the observations in Section 2.2, i.e. the convergence rate of the MPFA L-method is more sensitive to the grid regularity.

It should be mentioned that the situation of the TPFA method for both numerical examples above cannot be improved by refining the grid since the TPFA is inconsistent to the partial differential equation for the non-**K**-orthogonal grid.

5. CONCLUSIONS

This paper has presented the Dirichlet boundary influence on the MPFA L-method and the studies on the L-method in the case of homogeneous media. A new Dirichlet boundary discretization

DOI: 10.1002/fld

called 'full O' is proposed for the L-method and is compared with the Dirichlet boundary handling mentioned in [12, 17]. Numerical results of the three examples in Section 2.2 show that, in the case of convergence, the improper implementation of Dirichlet boundary will reduce the superconvergence rate of the L-method, especially for the normal velocity. However, compared with the influence of the grid shape on the superconvergence behavior, the boundary effect can be neglected. For a uniform grid, the new 'full O' strategy can significantly improve the superconvergence order of the normal velocity from $\mathcal{O}(h^{1.5})$ to $\mathcal{O}(h^2)$. For the special case of homogeneous media, the simplification of the L-method gives an equivalent description of the criterion for the choice of the L triangle by some geometrical information instead of by the transmissibility coefficients for the original criterion. That is, the L triangle with smaller absolute transmissibility coefficient that is chosen is equivalent to the L triangle with longer path along the direction of $\mathbf{K}^{\mathrm{T}}\mathbf{n}_e$ is chosen. This intuitive observation shows when the two L triangles corresponding to an entire cell edge are chosen in combination of $(\mathrm{T}_1, \mathrm{T}_3)$ or $(\mathrm{T}_2, \mathrm{T}_4)$, when in a combination of $(\mathrm{T}_1, \mathrm{T}_4)$ or $(\mathrm{T}_2, \mathrm{T}_3)$. Based on the above theoretical results, the reason for the big errors inside the quadrilateral grid (see Figure 9 (left)) is well interpreted, which indicates that the superconvergence behavior of the L-method is more sensitive to the shape of the grid compared with the O-method. The two-phase flow results show that it is quite important to choose the proper discretization method for the elliptic operators in the flow equation. Otherwise, a wrong pressure field causes a bad velocity field, which gives a completely wrong result for the saturation. We also observe that the TPFA method cannot converge to the correct solution for the general non-**K**-orthogonal grid even with the refinement of the grid as mentioned in Section 1. However, the MPFA L-method overcomes the inconsistency of the TPFA and works properly for multi-phase flow in reservoir simulation.

ACKNOWLEDGEMENTS

We would like to thank Prof. Ivar Aavatsmark for his helpful discussions. The authors are the members of the International Research Training Group NUPUS, financed by the German Research Foundation (DFG) and The Netherlands Organisation for Scientific Research (NWO), and thank the DFG (GRK 1398) and NWO (DN 81-754) for their support.

REFERENCES

1. Helmig R. *Multiphase Flow and Transport Processes in the Subsurface*. Springer: Berlin, 1997.
2. Aavatsmark I. Interpretation of a two-point flux stencil for skew parallelogram grids. *Computational Geosciences* 2007; **11**(3):199–206.
3. Aavatsmark I. Mehrpunktflussverfahren. *Technical Report*, Institut für Wasserbau, Universität Stuttgart, 2004.
4. Aavatsmark I, Barkve T, Bøe Ø, Mannseth T. Discretization on non-orthogonal, quadrilateral grids for inhomogeneous, anisotropic media. *Journal of Computational Physics* 1996; **127**:2–14.
5. Aavatsmark I, Barkve T, Mannseth T. Control volume discretization methods for 3D quadrilateral grids in inhomogeneous, anisotropic reservoirs. *SPE Journal* 1998; **3**:146–154.
6. Aavatsmark I. An introduction to multipoint flux approximations for quadrilateral grids. *Computational Geosciences* 2002; **6**:405–432.
7. Aavatsmark I, Eigestad GT, Klausen RA. Numerical convergence of the MPFA O-method for general quadrilateral grids in two and three dimensions. In *Compatible Spatial Discretizations*, Arnold DN, Bochev PB, Lehoucq RB, Nicolaides RA, Shashkov M (eds). IMA Volume Series. Springer: New York, 2006; 1–21.
8. Edwards MG, Rogers CF. Finite volume discretization with imposed flux continuity for the general tensor pressure equation. *Computational Geosciences* 1998; **2**:259–290.
9. Edwards MG. Unstructured, control-volume distributed, full-tensor finite-volume schemes with flow based grids. *Computational Geosciences* 2002; **6**:433–452.

DOI: 10.1002/fld

10. Aavatsmark I, Eigestad GT. Numerical convergence of the MPFA O-method and U-method for general quadrilateral grids. *International Journal for Numerical Methods in Fluids* 2006; **51**:939–961.
11. Aavatsmark I, Eigestad GT, Klausen RA, Wheeler MF, Yotov I. Convergence of a symmetric MPFA method on quadrilateral grids. *Computational Geosciences* 2007; **11**:333–345.
12. Eigestad GT, Klausen RA. On the convergence of the multi-point flux approximation O-method: numerical experiments for discontinuous permeability. *Numerical Methods for Partial Differential Equations* 2005; **21**: 1079–1098.
13. Klausen RA, Winther R. Convergence of multipoint flux approximations on quadrilateral grids. *Numerical Methods for Partial Differential Equations* 2006; **22**:1438–1454.
14. Klausen RA, Winther R. Robust convergence of multi point flux approximation on rough grids. *Numerische Mathematik* 2006; **104**:317–337.
15. Wheeler MF, Yotov I. A cell-centered finite difference method on quadrilaterals. In *Compatible Spatial Discretizations*, Arnold DN, Bochev PB, Lehoucq RB, Nicolaides RA, Shashkov M (eds). IMA Volume Series. Springer: New York, 2006; 189–207.
16. Nordbotten JM, Aavatsmark I, Eigestad GT. Monotonicity of control volume methods. *Numerische Mathematik* 2007; **106**:255–288.
17. Aavatsmark I, Eigestad GT, Mallison BT, Nordbotten JM. A compact multipoint flux approximation method with improved robustness. *Numerical Methods for Partial Differential Equations* 2008; **24**:1329–1360.
18. Aavatsmark I, Eigestad GT, Heimsund BO, Mallison BT, Nordbotten JM, Øian E. A new finite volume approach to efficient discretization on challenging grids. *Society of Petroleum Engineers Reservoir Simulation Symposium*, Texas, U.S.A., 2007.
19. Flemisch B, Fritz J, Helmig R, Niessner J, Wohlmuth B. DUMUX: a multi-scale multi-physics toolbox for flow and transport processes in porous media. In *ECCOMAS Thematic Conference on Multi-scale Computational Methods for Solids and Fluids*, Ibrahimbegovic A, Dias F (eds), Cachan, France, 2007; 82–87.
20. Bastian P, Blatt M, Dedner A, Engwer C, Klöfkorn R, Kornhuber R, Ohlberger M, Sander O. A generic grid interface for parallel and adaptive scientific computing. Part II: implementation and tests in DUNE. *Preprint*, *No. 404*, DFG Research Center MATHEON, 2007.
21. Schenk O, Gärtner K. Solving unsymmetric sparse systems of linear equations with PARDISO. *Journal of Future Generation Computer Systems* 2004; **20**:475–487.

DOI: 10.1002/fld